A Control-Oriented and Physics-Based Model for Ionic Polymer–Metal Composite Actuators

Zheng Chen, *Student Member, IEEE*, and Xiaobo Tan, *Member, IEEE*

***Abstract*—Ionic polymer–metal composite (IPMC) actuators have promising applications in biomimetic robotics, biomedical devices, and micro/nanomanipulation. In this paper, a physics-based model is developed for IPMC actuators, which is amenable to model reduction and control design. The model is represented as an infinite-dimensional transfer function relating the bending displacement to the applied voltage. It is obtained by exactly solving the governing partial differential equation in the Laplace domain for the actuation dynamics, where the effect of the distributed surface resistance is incorporated. The model is expressed in terms of fundamental material parameters and actuator dimensions, and is thus, geometrically scalable. To illustrate the utility of the model in controller design, an H_∞ controller is designed based on the reduced model and applied to tracking control. Experimental results are presented to validate the proposed model and its effectiveness in real-time control design.**

***Index Terms*—Electroactive polymers, ionic polymer–metal composite (IPMC) actuators, model-based control design, physics-based model.**

I. Introduction

IONIC polymer–metal composites (IPMCs) form an important category of electroactive polymers (also known as artificial muscles) and have built-in actuation and sensing capabilities [1], [2]. An IPMC sample typically consists of a thin ion-exchange membrane (e.g., Nafion), chemically plated on both surfaces with a noble metal as electrode [3]. Transport of hydrated cations and water molecules within an IPMC under an applied voltage and the associated electrostatic interactions lead to bending motions of the IPMC, and hence, the actuation effect. Fig. 1 illustrates the mechanism of the IPMC actuation. Because of their softness, resilience, biocompatibility, and the capability of producing large deformation under a low action voltage, IPMCs are very attractive for many applications in the fields of biomedical devices and biomimetic robots [4]–[10]. Microfabrication of IPMC [11] has also been reported, which extends IPMCs applications into micro- and nanomanipulation domains.

A faithful and practical model is desirable for real-time control of this novel material in various potential applications.

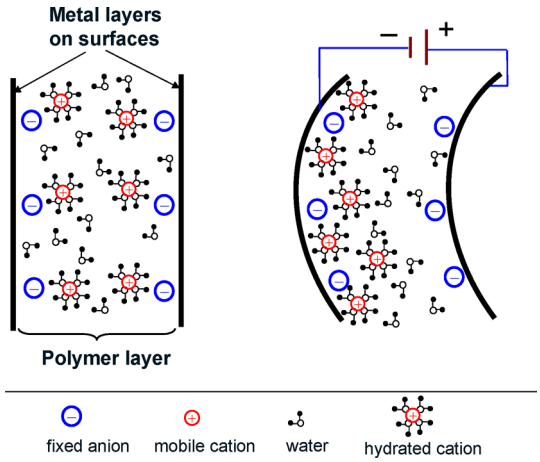

Fig. 1. Illustration of IPMC actuation mechanism.

Current modeling work can be classified into three categories based on their complexity levels. Based purely on the empirical responses, *black-box* models, e.g., [12] and [13], offer minimal insight into the governing mechanisms within the IPMC. While these models are simple in nature, they are often sample-dependent and not scalable in dimensions. As a more detailed approach, the *gray-box* models, e.g., [14]–[16], are partly based on physical principles while also relying on empirical results to define some of the more complex physical processes. In the most complex form, *white-box* models with partial differential equations (PDEs), e.g., [17]–[22], attempt to explain the underlying physics for the sensing and actuation responses of IPMCs, but they are not practical for real-time control purposes. In particular, Farinholt derived the impedance response for a cantilevered IPMC beam under step and harmonic voltage excitations [20]. The derivation was based on a linear, one-dimensional PDE governing the internal charge dynamics, which was first developed by Nemat-Nasser and Li for studying the actuation response of IPMCs [18].

In this paper, an explicit control-oriented yet physics-based actuation model for IPMC actuators is presented. The model combines the seemingly incompatible advantages of both the white-box models (capturing key physics) and the black-box models (amenable to control design). The proposed modeling approach provides an interpretation of the sophisticated physical processes involved in IPMC actuation from a systems perspective. The model development starts from the same governing PDE as in [18] and [20] that describes the charge redistribution dynamics under external electrical field, electrostatic interactions, ionic diffusion, and ionic migration along the thickness direction. The model extends the research in [18] and [20] by

Manuscript received June 15, 2007; revised February 14, 2008. Current version published October 8, 2008. Recommended by Technical Editor I-M. Chen. This work was supported in part by the National Science Foundation (NSF) under CAREER Grant ECCS 0547131 and in part by the Michigan State University (MSU) Intramural Research Grant Program (IRGP) under Grant 05-IRGP-418.

The authors are with the Department of Electrical and Computer Engineering, Michigan State University, East Lansing, MI 48824 USA (e-mail: chenzhe1@egr.msu.edu; xbtan@egr.msu.edu).

Color versions of one or more of the figures in this paper are available online at http://ieeexplore.ieee.org.

Digital Object Identifier 10.1109/TMECH.2008.920021

incorporating the effect of distributed surface resistance, which is known to influence the actuation behavior of IPMCs [23], [24]. Moreover, by converting the original PDE into the Laplace domain, an exact solution is obtained, leading to a compact, analytical model in the form of infinite-dimensional transfer function. The model can be further reduced to low-order models, which again carry physical interpretations and are geometrically scalable.

Experiments have been conducted to validate the proposed dynamic model for IPMC actuators in a cantilevered configuration. Good agreement, both in magnitude and in phase, has been achieved between the experimental measurement and the model prediction for the impedance response from 0.02 to 100 Hz, and for bending response from 0.02 to 20 Hz. The results show that considering the surface resistance leads to more accurate predictions. The geometric scalability of the actuator model has also been confirmed without retuning of the identified physical parameters.

An example is further provided to illustrate the use of the proposed model for controller development, where an H_∞ controller is designed based upon a reduced model. Experimental results on tracking control have shown that model-based H_∞ controller ensures internal stability and tracking precision in the presence of measurement noises and model uncertainties while taking into account control effort consumption.

The remainder of the paper is organized as follows. The governing PDE is reviewed in Section II. In Section III, the electrical impedance model for IPMC actuator is derived by exactly solving the PDE, with and without considering the surface resistance. This lays the groundwork for deriving the full actuation model, which is described in Section IV. Model reduction is discussed in Section V. Experimental validation of the proposed model is presented in Section VI. Model-based H_∞ controller design and its real-time implementation are reported in Section VII. Finally, concluding remarks are provided in Section VIII.

II. Governing PDE

The governing PDE for charge distribution in an IPMC was first presented in [18] and then used by Farinholt [20] for investigating the actuation and sensing response. Let $\mathbf{D}$, $\mathbf{E}$, ϕ, and ρ denote the electric displacement, the electric field, the electric potential, and the charge density, respectively. The following equations hold:

$$\mathbf{E} = \frac{\mathbf{D}}{\kappa_e} = -\nabla\phi \tag{1}$$

$$\nabla \cdot \mathbf{D} = \rho = F(C^+ - C^-) \tag{2}$$

where κ_e is the effective dielectric constant of the polymer, F is Faraday's constant, and C^+ and C^- are the cation and anion concentrations, respectively. The continuity equation is given by

$$\nabla \cdot \mathbf{J} = -\frac{\partial C^+}{\partial t} \tag{3}$$

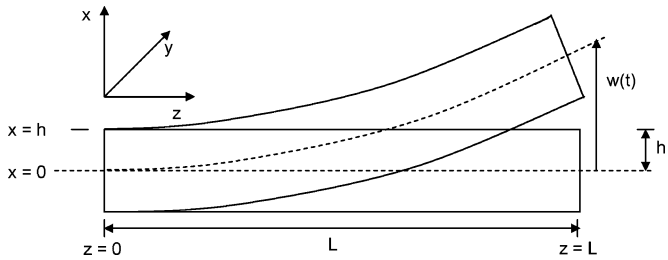

Fig. 2. Geometric definitions of an IPMC cantiliver beam.

where $\mathbf{J}$ is the ion flux vector. Since the thickness of an IPMC is much smaller than its length or width, one can assume that, inside the polymer, $\mathbf{D}$, $\mathbf{E}$, and $\mathbf{J}$ are all restricted to the thickness direction (x-direction). This enables one to drop the boldface notation for these variables. The ion flux consists of diffusion, migration, and convection terms

$$J = -d\left(\nabla C^+ + \frac{C^+F}{RT}\nabla\phi + \frac{C^+\Delta V}{RT}\nabla p\right) + C^+ v \tag{4}$$

where d is the ionic diffusivity, R is the gas constant, T is the absolute temperature, p is the fluid pressure, v is the free solvent velocity field, and ΔV is the volumetric change. Considering Darcy's law and ignoring the nonlinear terms in (4) (see [25] for justification), the PDE for charge density can be derived as

$$\frac{\partial \rho}{\partial t} - d\frac{\partial^2 \rho}{\partial x^2} + \frac{F^2 d C^-}{\kappa_e RT}\left(1 - C^-\Delta V\right)\rho = 0. \tag{5}$$

Nemat-Nasser and Li [18] assumed that the induced stress is proportional to the charge density

$$\sigma = \alpha_0 \rho \tag{6}$$

where α_0 is the coupling constant.

Farinholt [20] investigated the current response of a cantilevered IPMC beam when the base is subject to step and harmonic actuation voltages. A key assumption is that the ion flux at the polymer/metal interface is zero. This assumption, which serves as a boundary condition for (5), leads to

$$\left(\frac{\partial^3 \phi}{\partial x^3} - \frac{F^2 C^-}{\kappa_e RT}\left(1 - C^-\Delta V\right)\frac{\partial \phi}{\partial x}\right)|_{x=\pm h} = 0. \tag{7}$$

While the work in [20] represents an important progress in IPMC modeling, it cannot be used for model-based controller design. The latter is the main motivation of this paper.

III. Electrical Impedance Model

From (6), the stress induced by the actuation input is directly related to the charge density distribution ρ. Therefore, as a first step in developing the actuation model, we will derive the electrical impedance model in this section. While the latter is of interest in its own right, one also obtains the explicit expression for ρ as a byproduct of the derivation.

Consider Fig. 2, where the beam is clamped at one end ($z = 0$) and is subject to an actuation voltage producing the tip displacement $w(t)$ at the other end ($z = L$). The neutral axis of the

beam is denoted by $x = 0$, and the upper and lower surfaces are denoted by $x = h$ and $x = -h$, respectively.

To ease the presentation, define the aggregated constant

$$K \triangleq \frac{F^2 dC^-}{\kappa_e RT}\left(1 - C^- \Delta V\right). \tag{8}$$

Performing Laplace transform for the time variable of $\rho(x, z, t)$ (noting the independence of ρ from the y coordinate), one converts (5) into the Laplace domain

$$s\rho\left(x, z, s\right) - d\frac{\partial^2 \rho\left(x, z, s\right)}{\partial x^2} + K\rho\left(x, z, s\right) = 0 \tag{9}$$

where s is the Laplace variable. Define $\beta(s)$ such that $\beta^2 = (s + K)/d$. With an assumption of symmetric charge distribution about $x = 0$, a generic solution to (9) can be obtained as

$$\rho(x, z, s) = 2c_2(z, s)\sinh\left(\beta(s)x\right) \tag{10}$$

where $c_2(z, s)$ depends on the boundary condition of the PDE. Using (10) and the field equations (1) and (2), one can derive the expressions for the electric field E and then for the electric potential ϕ in the Laplace domain

$$E(x, z, s) = 2c_2(z, s)\frac{\cosh\left(\beta(s)x\right)}{\kappa_e \beta(s)} + a_1(z, s) \tag{11}$$

$$\phi(x, z, s) = -2c_2(z, s)\frac{\sinh\left(\beta(s)x\right)}{\kappa_e \beta^2(s)} - a_1(z, s)x + a_2(z, s) \tag{12}$$

where $a_1(z, s)$ and $a_2(z, s)$ are appropriate functions to be determined based on the boundary conditions on ϕ. Two different boundary conditions are discussed next, one ignoring the surface electrode resistance and the other considering the resistance. In both cases, it will be shown that the final actuation current is proportional to the applied voltage input $V(s)$, and thus, a transfer function for the impedance model can be derived.

A. Model Ignoring the Surface Resistance

First consider the case where the surface electrodes are perfectly conducting, as was assumed by Farinholt [20]. The electric potential is uniform across both surfaces $x = \pm h$, and without loss of generality, the potential is set to be

$$\phi\left(\pm h, z, s\right) = \frac{\pm V\left(s\right)}{2}. \tag{13}$$

Combining (12) and (13) with (7), one can solve for $a_1(z, s)$, $a_2(z, s)$, and $c_2(z, s)$, and then obtain $E(h, z, s)$ from (11)

$$E\left(h, z, s\right) = -\frac{V\left(s\right)}{2h}\frac{\gamma\left(s\right)\left(s + K\right)}{\left(s\gamma\left(s\right) + K\tanh\left(\gamma\left(s\right)\right)\right)} \tag{14}$$

where $\gamma(s) \triangleq \beta(s)h$. The total charge is obtained by integrating the electrical displacement D on the boundary $x = h$

$$Q(s) = \int_0^W \int_0^L D(h, z, s)dz\, dy = \int_0^W \int_0^L \kappa_e E(h, z, s)dz\, dy. \tag{15}$$

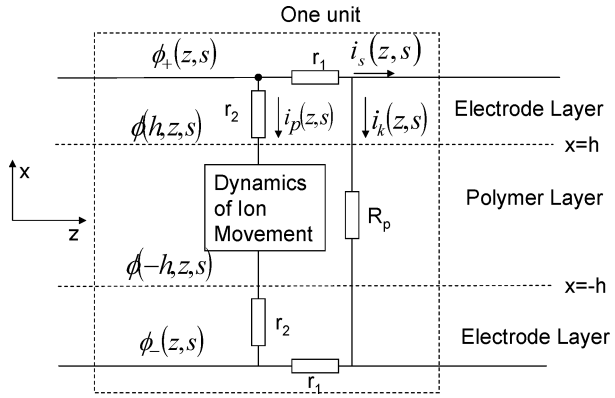

Fig. 3. Illustration of the IPMC impedance model with surface resistance.

Plugging (14) into (15), one can derive $Q(s)$, which is linear with respect to the external stimulus $V(s)$. The actuation current $i(t)$ is the time-derivative of the charge $Q(t)$, and hence, $I(s) = sQ(s)$ in the Laplace domain. The impedance is then derived as

$$Z_1\left(s\right) = \frac{V\left(s\right)}{I\left(s\right)} = \frac{s + K(\tanh\left(\gamma\left(s\right)\right)/\gamma\left(s\right))}{Cs\left(s + K\right)} \tag{16}$$

where $C = \kappa_e WL/(2h)$ can be regarded as the capacitance of the IPMC.

B. Model Considering Distributed Surface Resistance

The surface electrode of an IPMC typically consists of aggregated nanoparticles formed during chemical reduction of noble metal salt (such as platinum salt) [3]. The surface resistance is thus nonnegligible and has an influence on the sensing and actuation behavior of an IPMC [23]. In this paper, the effect of distributed surface resistance is incorporated into the impedance model, as illustrated in Fig. 3. Let the electrode resistance per unit length be r_1 in z direction and r_2 in x direction. One can further define these quantities in terms of fundamental physical parameters: $r_1 = r_1'/W$, $r_2 = r_2'/W$, with r_1' and r_2' representing the surface resistance per $\{$unit length $\cdot$ unit width$\}$ in z and x directions, respectively. In Fig. 3, $i_p(z, s)$ is the distributed current per unit length going through the polymer due to the ion movement, $i_k(z, s)$ represents the leaking current per unit length, and $i_s(z, s)$ is the surface current on the electrodes. R_p denotes the through-polymer resistance per unit length, which can be written as $R_p = R_p'/W$, with R_p' being the polymer resistance per $\{$unit length $\cdot$ unit width$\}$. Note that by the continuity of current, the current $i_s(z, s)$ on the top surface equals that on the bottom surface but with an opposite direction. The surface current $i_s(0, s)$ at $z = 0$ is the total actuation current $i(s)$.

The following equations capture the relationships between $i_s(z, s)$, $i_p(z, s)$, $i_k(z, s)$, $\phi_\pm(z, s)$:

$$\frac{\partial \phi_\pm(z, s)}{\partial z} = \mp\frac{r_1'}{W} i_s(z, s) \tag{17}$$

$$\frac{\partial i_s(z, s)}{\partial z} = -(i_p(z, s) + i_k(z, s)). \tag{18}$$

From the potential condition at $z=0$, i.e., $\phi_{\pm}(0,s)=\pm V(s)/2$, the boundary conditions for (12) are derived as

$$\phi(\pm h,z,s)=\phi_{\pm}(z,s)\mp i_p(z,s)r_2'/W. \tag{19}$$

With (17) and (19), one gets

$$\phi\left(\pm h,z,s\right)=\frac{\pm V\left(s\right)}{2}\mp\int_0^z\frac{r_1'}{W}i_s\left(\tau,s\right)d\tau-\frac{r_2'}{W}i_p\left(z,s\right). \tag{20}$$

Combining (20) with (12), one can solve for the functions $a_1(z,s)$ and $a_2(z,s)$ in the generic expression for $\phi(x,z,s)$. With consideration of the boundary condition (7), one can solve for $c_2(z,s)$. With $a_1(z,s)$, $a_2(z,s)$, and $c_2(z,s)$, one obtains $E(h,z,s)$ from (11)

$$E\left(h,z,s\right)=-\frac{\phi\left(h,z,s\right)}{h}\frac{\gamma\left(s\right)\left(s+K\right)}{\gamma\left(s\right)s+K\tanh\left(\gamma\left(s\right)\right)}. \tag{21}$$

Define the actuation current along the negative x-axis direction to be positive. The current i_p due to the ion movement can be obtained as

$$i_p\left(z,s\right)=-sWD\left(h,z,s\right)=-sW\kappa_eE\left(h,z,s\right). \tag{22}$$

The leaking current i_k can be obtained as

$$i_k\left(z,s\right)=\frac{\phi_+\left(z,s\right)-\phi_-\left(z,s\right)}{R_p'/W}. \tag{23}$$

With (21)–(23), one can solve the PDE (18) for the surface current $i_s(z,s)$ with the boundary condition $i_s(L,s)=0$. The total actuation current $I(s)=i_s(0,s)$ can be obtained, from which the transfer function for the impedance can be shown to be

$$Z_2\left(s\right)=\frac{V\left(s\right)}{I\left(s\right)}=\frac{2\sqrt{B\left(s\right)}}{A\left(s\right)\tanh\left(\sqrt{B\left(s\right)}L\right)} \tag{24}$$

where

$$A\left(s\right)\triangleq\frac{\theta\left(s\right)}{\left(1+r_2'\theta\left(s\right)/W\right)}+\frac{2W}{R_p'} \tag{25}$$

$$B\left(s\right)\triangleq\frac{r_1'}{W}A\left(s\right) \tag{26}$$

$$\theta\left(s\right)\triangleq\frac{sW\kappa_e\gamma\left(s\right)\left(s+K\right)}{h\left(s\gamma\left(s\right)+K\tanh\left(\gamma\left(s\right)\right)\right)}. \tag{27}$$

See Appendix I for the detailed derivation.

One can show that $Z_2(s)$ is consistent with $Z_1(s)$ (16), when $r_1'\to 0$, $r_2'\to 0$, and $R_p'\to\infty$.

IV. Actuation Model

First, we derive the transfer function $H(s)$ relating the free tip displacement of an IPMC beam, $w(L,s)$, to the actuation voltage $V(s)$, when the beam dynamics (inertia, damping, etc.) is ignored. From (6) and (10), one obtains the generic expression for the stress $\sigma(x,z,s)$ generated due to actuation

$$\sigma(x,z,s)=2\alpha_0c_2(z,s)\sinh\left(\beta(s)x\right). \tag{28}$$

Note that $c_2(z,s)$ is available from the derivation of the impedance model. When considering the surface resistance, the bending moment $M(z,s)$ is obtained as

$$\begin{aligned}M\left(z,s\right)&=\int_{-h}^{h}x\sigma\left(x,z,s\right)W\,dx\\&=\int_{-h}^{h}2\alpha_0Wxc_2(z,s)\sinh\left(\beta(s)x\right)dx\\&=-\frac{2\alpha_0KW\kappa_e\left(\gamma\left(s\right)-\tanh\left(\gamma\left(s\right)\right)\right)\phi\left(h,z,s\right)}{\left(s\gamma\left(s\right)+K\tanh\left(\gamma\left(s\right)\right)\right)}.\end{aligned} \tag{29}$$

From the linear beam theory [26]

$$\begin{aligned}\frac{\partial^2w\left(z,s\right)}{\partial z^2}&=\frac{M\left(z,s\right)}{YI}\\&=-\frac{2\alpha_0KW\kappa_e\left(\gamma\left(s\right)-\tanh\left(\gamma\left(s\right)\right)\right)\phi\left(h,z,s\right)}{YI\left(s\gamma\left(s\right)+K\tanh\left(\gamma\left(s\right)\right)\right)}\\&=-\frac{\alpha_0KW\kappa_e\left(\gamma\left(s\right)-\tanh\left(\gamma\left(s\right)\right)\right)}{YI\left(s\gamma\left(s\right)+K\tanh\left(\gamma\left(s\right)\right)\right)}\\&\quad\times\frac{V(s)-2\int_0^z(r_1'/W)i_s\left(\tau,s\right)d\tau}{1+r_2'\theta\left(s\right)/W}\end{aligned} \tag{30}$$

where the last equality follows from (20) and (51), Y is the effective Young's modulus of the IPMC, and $I=2/3Wh^3$ is the moment of inertia of the IPMC. Solving (30) with boundary conditions $w(0,s)=0$ and $w'(0,s)=0$, one can get

$$\begin{aligned}w\left(L,s\right)&=-\frac{1}{2}\frac{\alpha_0W}{YI}\frac{K\kappa_e\left(\gamma\left(s\right)-\tanh\left(\gamma\left(s\right)\right)\right)}{\left(\gamma\left(s\right)s+K\tanh\left(\gamma\left(s\right)\right)\right)}\\&\quad\times\frac{V\left(s\right)L^2-4\int_0^L\int_0^z\int_0^{z'}r_1'/Wi_s\left(\tau,s\right)d\tau\,dz'\,dz}{1+r_2'\theta\left(s\right)/W}.\end{aligned}$$

Using (52) and (53), one can show

$$V\left(s\right)L^2-4\int_0^L\int_0^z\int_0^{z'}\frac{r_1'}{W}i_s\left(\tau,s\right)d\tau\,dz'\,dz=2L^2X(s)V(s)$$

where $X(s)$ is defined as

$$X\left(s\right)\triangleq-\frac{1-\operatorname{sech}\left(\sqrt{B(s)}L\right)-\tanh\left(\sqrt{B(s)}L\right)\sqrt{B\left(s\right)}L}{B\left(s\right)L^2}. \tag{31}$$

One thus obtains the transfer function $H(s)=w(L,s)/V(s)$. Hence

$$\begin{aligned}H\left(s\right)&=-\frac{L^2\alpha_0W}{2YI}\frac{K\kappa_e\left(\gamma\left(s\right)-\tanh\left(\gamma\left(s\right)\right)\right)}{\left(\gamma\left(s\right)s+K\tanh\left(\gamma\left(s\right)\right)\right)}\\&\quad\times\left(\frac{2X\left(s\right)}{1+r_2'\theta\left(s\right)/W}\right).\end{aligned} \tag{32}$$

$H(s)$ for the case where the surface resistance is ignored can be derived in an analogous and simpler manner, and it is omitted here for brevity. Note that the blocking force output $F(s)$ at the tip can be derived via $F(s)=w(L,s)K_0$, where $K_0=3YI/L^3$ denotes the spring constant of the beam.

Back to the free bending case, in order to accommodate the vibration dynamics of the beam, we cascade $G(s)$ to $H(s)$, as illustrated in Fig. 4. As the output of $G(s)$ represents the bending displacement (as that of $H(s)$ does), $G(s)$ will have a

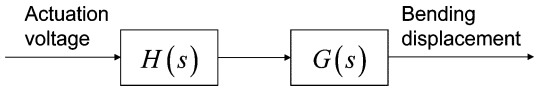

Fig. 4. Actuation model structure.

TABLE I
PARAMETERS FOR THE IMPEDANCE MODEL

F	R	T	R'_p
96487 C/mol	8.3143 J/mol · K	300 K	0.37 Ω · m^2
Y [10]	h	r'_1	r'_2
5.71×10^8 Pa	180 (μm)	22.3 Ω	1.8×10^{-5} Ω· m
d	C^-	κ_e	
1.38×10^{-9} m^2/s	1091 mol/m^3	1.34×10^{-6} F/m	

dc gain of 1. Since the actuation bandwidth of an IPMC actuator is relatively low (under 10 Hz), it often suffices to capture the mechanical dynamics $G(s)$ with a second-order system (first vibration mode)

$$G(s) = \frac{\omega_n^2}{s^2 + 2\xi\omega_n s + \omega_n^2} \tag{33}$$

where ω_n is the natural frequency of the IPMC beam and ξ is the damping ratio. The natural frequency ω_n can be further expressed in terms of the beam dimensions and mechanical properties [27].

V. Model Reduction

An important motivation for deriving a transfer function-type actuation model is its potential use for real-time feedback control. For practical implementation of feedback control design, the model needs to be finite-dimensional, i.e., being a finite-order, rational function of s. However, in the actuation model derived earlier, $H(s)$ is infinite-dimensional since it involves nonrational functions including $\sinh(\cdot)$, $\cosh(\cdot)$, $\sqrt{\cdot}$, etc. A systematic approach to model reduction is Padé approximation [28], where one can approximate $H(s)$ with a rational function of specified order. However, the computation involved is lengthy and the resulting coefficients for the reduced model can be complex. Therefore, in this paper a much simpler, alternative approach is proposed for model reduction by exploiting the knowledge of physical parameters and specific properties of hyperbolic functions.

For ease of presentation, decompose $H(s)$ as

$$H(s) = f(s) \cdot g(s) \cdot X(s)$$

where

$$f(s) = -\frac{L^2\alpha_0 W}{2YI}\frac{K\kappa_e(\gamma(s) - \tanh(\gamma(s)))}{(\gamma(s)s + K\tanh(\gamma(s)))} \tag{34}$$

$$g(s) = \frac{2}{1 + r'_2\theta(s)/W}. \tag{35}$$

Based on the physical parameters (see Table I in Section VI), $|\gamma(s)| \gg 10$, and $K \gg 10^6$, which allows one to make the approximation in the low-frequency range (<100 Hz)

$$\tanh(\gamma(s)) \approx 1 \tag{36}$$

$$\gamma(s) \approx h\sqrt{\frac{K}{d}} =: \gamma. \tag{37}$$

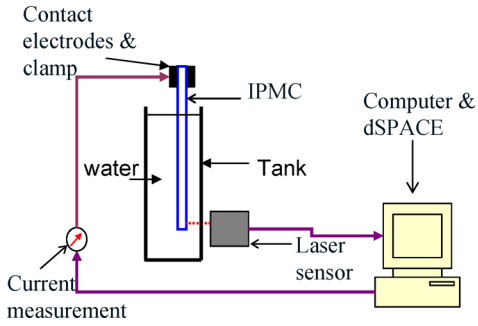

Fig. 5. Experimental setup.

With (36) and (37), one can simplify $f(s)$, $\theta(s)$, and $g(s)$ as

$$f(s) \approx -\frac{L^2\alpha_0 W}{2YI}\frac{K\kappa_e(\gamma - 1)}{(\gamma s + K)} \tag{38}$$

$$\theta(s) \approx \frac{sW\kappa_e\gamma(s + K)}{h(\gamma s + K)} \tag{39}$$

$$g(s) \approx \frac{2h(\gamma s + K)}{r'_2\gamma\kappa_e s(s + K) + h(\gamma s + K)}. \tag{40}$$

The Taylor series expansions of $\sinh(a)$ and $\cosh(a)$ will be used for approximating $X(s)$

$$X(s) \approx \frac{1 + \sum_{n=0}^{m}\left(a^{2n+2}/(2n+1)! - a^{2n}/(2n)!\right)}{\sum_{n=0}^{m} a^{2n+2}/(2n)!} \tag{41}$$

with $a = \sqrt{B(s)}L$, for some finite integer m. When $|s|$ is small (low-frequency range) and $2r'_1/R'_p$ is small (which is indeed the case, see parameters in Table I), $|\sqrt{B(s)}L|$ is small and (41) approximates $X(s)$ well with a small integer m. Note that only even-degree terms appear in (41), and hence (41) is a function of $B(s)L^2$ instead of $\sqrt{B(s)}L$. Finally, since $B(s)$ is a rational function of $\theta(s)$ and $\theta(s)$ is approximated by a rational function (39), one can obtain an approximation to $X(s)$ by a rational function of s.

Combining (38) and (40) and the approximation to $X(s)$, one gets a rational approximation to $H(s)$. Since the mechanical dynamics $G(s)$ is already rational, one obtains a finite-dimensional actuation model. Note that a reduced model is still a physical model. In particular, it is described in terms of fundamental physical parameters, and is thus, geometrically scalable. This represents a key difference from other low-order, black-box models, in which case the parameters have no physical meanings and one would have to reidentify the parameters empirically for every actuator.

VI. Experimental Model Verification

A. Experimental Setup

Fig. 5 shows the experimental setup. An IPMC sample is dipped in water and clamped at one end. The IPMC is subject to voltage excitation generated from the computer (through dSPACE DS1104 and ControlDesk). A laser displacement sensor (OADM 20I6441/S14F, Baumer Electric) with precision set to ±0.02 mm is used to measure the bending displacement $w(t)$.

The IPMC actuation current is measured with a current-amplifier circuit.

B. Identification of Parameters in Impedance Model

Table I lists the parameters obtained for the impedance model. Among them some are physical constants (gas constant R and Faraday's constant F), some can be measured directly (absolute temperature T, effective Young's modulus Y [10], actuator dimensions, surface resistance r_1 in z direction and through-polymer resistance R_p), and the others need to be identified through curve-fitting. Since $|C^-\Delta V| \ll 1$ [18], we take $1 - C^-\Delta V \approx 1$. The IPMC materials used in this paper were obtained from Environmental Robots Inc., and the sample dimensions reported have an accuracy of ± 0.5 mm in the length and width directions and ± 0.5 μm in the thickness direction.

A nonlinear fitting process is used to identify the diffusion coefficient d, the anion concentration C^-, the dielectric constant κ_e, and the surface resistance density r_2' in x direction, based upon the empirical impedance response of an IPMC actuator with dimensions 37.0 mm $\times$ 5.5 mm. In particular, the impedance model $Z_2(j2\pi f)$ predicts the magnitude and phase response of the actuator at frequency f, as a nonlinear function of the parameters. The Matlab function *fminsearch* can be used to find the parameters that minimize the squared error between the empirical frequency response and the model prediction. The identified parameters are listed in Table I, where the values of d and C^- are close to what were reported in the literature [20], [25]. The value of κ_e, however, differs from those reported in [20] and [25] by several orders of magnitude. This could be attributed to different materials and experimental conditions (e.g., in water versus in air). It should be noted that the value of κ_e in the relevant literature was also obtained through model fitting instead of direct physical measurement. It is thus of interest to examine more direct measurement of these parameters in the future.

For independent verification of the proposed model, the identified parameters will be used in predicting impedance behaviors of other IPMC actuators with different dimensions, as will be seen in Section VI-C.

C. Verification of Impedance Model

Impedance model verification will be conducted on two aspects. First, it will be shown that the model considering the surface resistance is more accurate than the model ignoring the resistance, by comparing them with the measured frequency response of an IPMC actuator. Second, the geometric scalability of the proposed model will be confirmed by the agreement between model predictions and experimental results for IPMC actuators with different dimensions.

1) Effect of Surface Resistance: In order to examine the difference between the impedance models $Z_1(s)$ and $Z_2(s)$, their model parameters were identified separately through the nonlinear fitting process described in Section VI-B. The experimental data were obtained for an IPMC actuator with dimensions 37.0 mm $\times$ 5.5 mm $\times$ 0.360 mm. Fig. 6 compares the predicted frequency response (both magnitude and phase) by each model

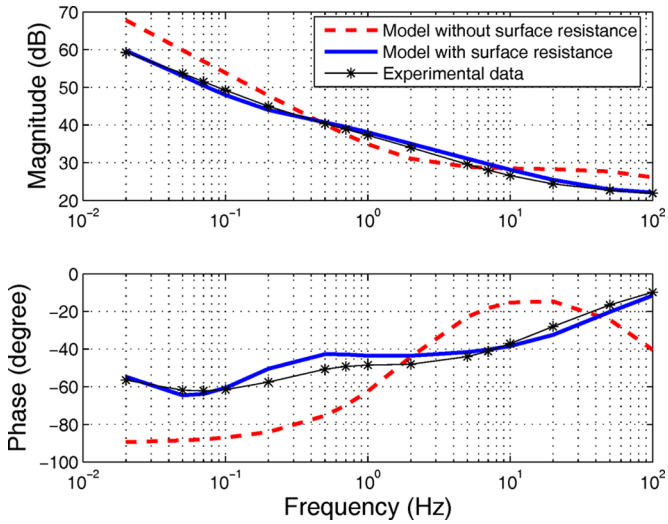

Fig. 6. Comparison of experimental impedance responses with model predictions, with and without consideration of surface resistance.

TABLE II
DIMENSIONS OF THREE IPMC SAMPLES USED FOR VERIFICATION OF MODEL SCALABILITY

IPMC beam	length (mm)	width (mm)	thickness (μm)
Big	39.0	11.0	360
Slim	37.0	5.5	360
Short	27.0	5.5	360

with the measured frequency response. It is clear that the model considering the surface resistance shows better agreement than the one ignoring the resistance. This indicates that the model incorporating the surface resistance is more effective in capturing the actuation dynamics of IPMC, and thus, it will be used for the remainder of this paper.

2) Geometric Scalability of the Dynamic Model: Three samples with different dimensions (see Table II) were cut from one IPMC sheet, and were labeled as *Big*, *Slim*, and *Short* for ease of referencing. The model parameters were first identified for the *Slim* sample, as discussed in Section VI-B. Without retuning, these parameters (except geometric dimensions) were plugged into (24), i.e., the model $Z_2(s)$, for predicting the frequency response for the *Big* and *Short* samples.

Fig. 7 shows the Bode plots of the frequency responses for the *Slim* and *Big* samples. It can be seen that for both samples, good agreement between the model prediction and the experimental data is achieved. Fig. 8 compares the frequency responses of the *Slim* and *Short* samples. Reasonable match between the model predictions and the empirical curves is again achieved for both samples. These figures show that the model is geometrically scalable.

D. Verification of Actuation Model

The actuation model has two modules serially connected, as shown in Fig. 4. All parameters of $H(s)$ have been identified during identification of the impedance model except the stress–charge coupling constant α_0. The natural frequency ω_n and the damping ratio ξ in $G(s)$ can be identified based on the

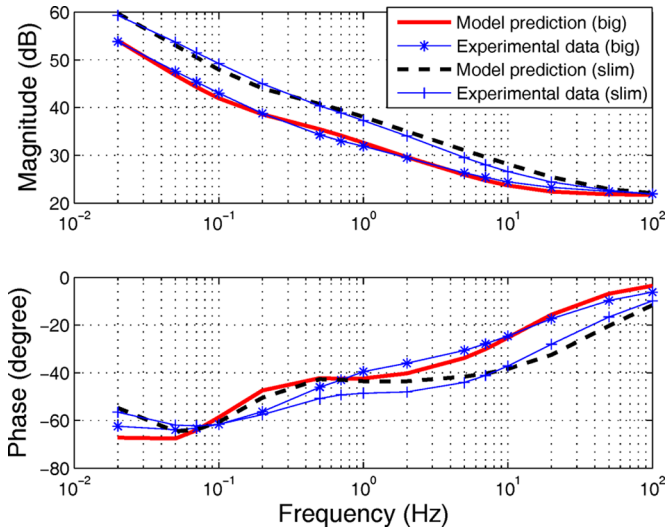

Fig. 7. Impedance model verification for the *Big* and *Slim* IPMC samples.

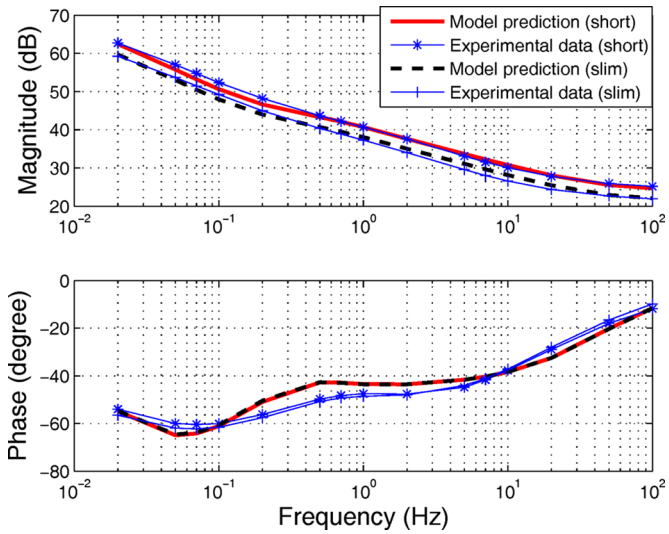

Fig. 8. Impedance model verification for the *Slim* and *Short* IPMC samples.

measurement of damped oscillations of the IPMC beam in the passive state. For the *Big* sample, we obtained $\omega_n = 28.9$ rad/s, and $\xi = 0.1$. Finally, α_0, which is simply a gain parameter in the actuation model, was identified to be $\alpha_0 = 0.129$ J/C using the magnitude of actuation response measured under a sinusoidal voltage input.

The whole actuation model was verified in experiments by applying sinusoidal actuation signals $V(t)$ with amplitude 0.2 V and frequency from 0.02 to 20 Hz. The laser sensor was used to measure the bending displacement $w(t)$ at the free end of the *Big* sample. The magnitude gain and phase shift from the input $V(s)$ to the output $w(s)$ were obtained, which show good agreement with the model prediction; see Fig. 9. Note that, from the empirical Bode plot, the natural frequency of the IPMC beam in the active state (under actuation) is about 30 rad/s, and thus, slightly higher than that measured in the passive state. It indicates that the effective stiffness of an IPMC is influenced by the actuation input. However, such an effect is not significant

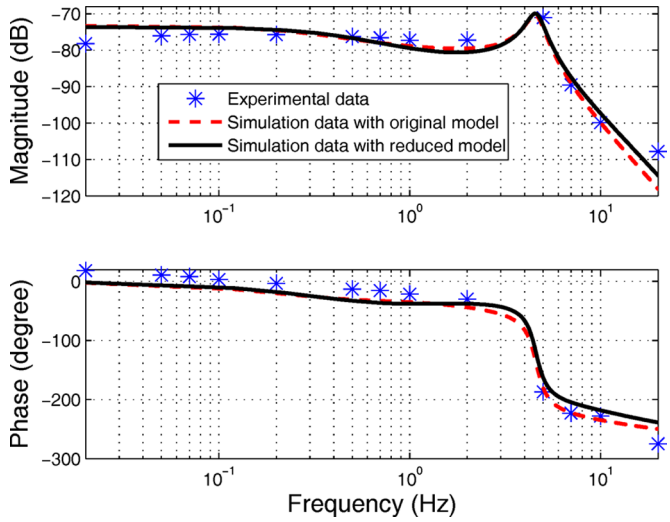

Fig. 9. Comparison of the measured actuation response with the proposed full and reduced models for the *Big* sample.

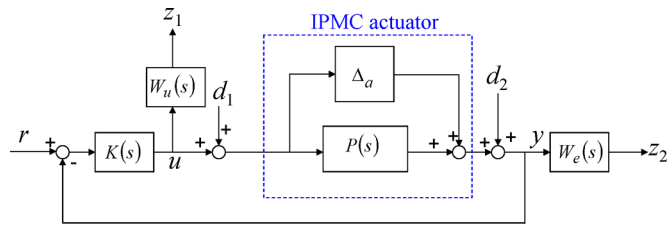

Fig. 10. Schematic of the closed-loop control system for an IPMC actuator.

for relatively low actuation voltages, and a detailed discussion on this would be beyond the scope of the current paper.

Model reduction was then carried out for $H(s)$ using the techniques discussed in Section V, where $m = 2$ was used. This resulted in a seventh-order model $\hat{H}_1(s)$ for approximating $H(s)$. The Matlab command *reduce* was further used to reduce $\hat{H}_1(s)$ to a second-order function $\hat{H}(s)$, which leads to a fourth-order reduced model for the overall actuation response for the *Big* sample

$$P(s) = \hat{H}(s) \cdot G(s) = \frac{0.005s + 0.043}{s^2 + 78s + 204} \cdot \frac{835}{s^2 + 5.78s + 835}. \tag{42}$$

From Fig. 9, the reduced model also matches closely the empirical response. It will be used for model-based controller design in the next section.

VII. Controller-Design Example: Model-Based H_∞ Control

In this section, we provide an example to illustrate the use of the proposed model in model-based controller design. While other control design methodologies can be adopted, H_∞ control has been chosen to accommodate multiple considerations, including stability in the presence of uncertainty, attenuation of the effect of sensing noise, and minimization of control effort.

Consider Fig. 10, where the IPMC is represented by some nominal model $P(s)$ with an additive uncertainty Δ_a. Let $P(s)$

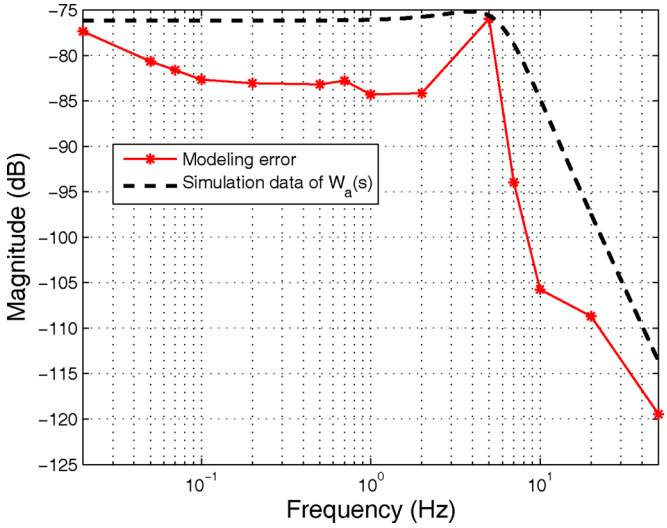

Fig. 11. Modeling error and its bound $W_a(s)$.

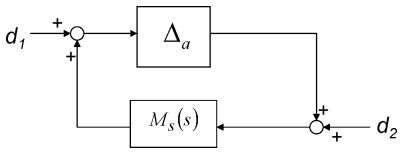

Fig. 12. The feedback connection of $M_s(s)$ and $\Delta_a(s)$.

be the reduced model (42) for the *Big* sample. Then Δ_a represents the error between the full actuation model and $P(s)$ plus the unmodeled nonlinearities. The signals d_1 and d_2 denote the actuation noise and the sensing noise, respectively. One is interested in designing a controller $K(s)$ that ensures closed-loop stability and robust tracking performance in the presence of Δ_a and the noises d_1 and d_2 while taking into account the consumed control effort. Standard H_∞ control techniques [29] are used in the following controller design.

To ensure the closed-loop stability in the presence of Δ_a, one needs to first obtain the bound $\|\Delta_a\|_\infty$. Fig. 11 shows the modeling error—the difference between the measured response and $P(s)$, as well as a bound $W_a(s)$ on the error, where

$$W_a(s) = \frac{0.15}{s^2 + 37s + 1318}. \tag{43}$$

Then $\|\Delta_a\|_\infty \le \|W_a(s)\|_\infty = 1.65 \times 10^{-4}$.

The closed-loop system in Fig. 10 can be regarded as the feedback connection of Δ_a and $M_s(s)$, as illustrated in Fig. 12. $M_s(s)$ can be obtained by computing the transfer function from the output of Δ_a to the input of Δ_a in Fig. 10

$$M_s(s) = \frac{K(s)}{1 + P(s)K(s)}. \tag{44}$$

From the small gain theorem [29], a sufficient condition for internal stability is

$$\|M_s(s)\|_\infty < \frac{1}{\|W_a(s)\|_\infty} = 6038. \tag{45}$$

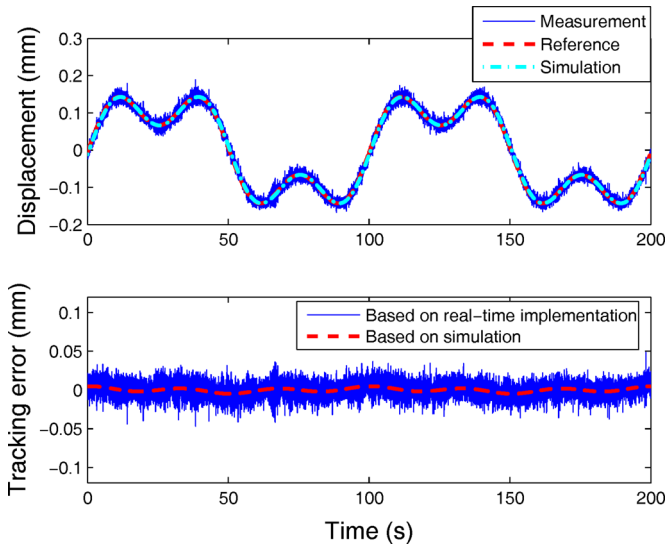

Fig. 13. Experimental and simulation results on tracking of IPMC actuator under H_∞ control.

To proceed with the controller design, define two artificial outputs z_1 and z_2 as in Fig. 10, where the performance weight $W_e(s)$ and the control weight $W_u(s)$ are chosen to be

$$W_e(s) = \frac{s + 124}{4(s + 3.1 \times 10^{-3})}, \quad W_u(s) = \frac{100(s + 0.24)}{s + 3.4 \times 10^5}.$$

For guidelines on choosing these weight functions, see [29]. Now ignore the Δ_a block, and design $K(s)$ to minimize the H_∞ norm of the transfer function from $\{d_1, d_2\}^T$ to $\{z_1, z_2\}^T$. This would minimize the effect of the noises on the tracking performance and the control effort. The resulting controller is

$$K(s) = \frac{29527(s + 2.569)}{(s + 0.00314)(s + 4.952)}.$$

From (44), one can calculate $\|M_s(s)\|_\infty = 5395$, which satisfies the internal stability condition (45) under the uncertainty.

The designed H_∞ controller was implemented for tracking control of the *Big* IPMC sample, where the reference r (in millimeter) used was

$$r(t) = 0.133 \sin(0.02\pi t) + 0.0665 \sin(0.06\pi t).$$

The laser sensor for measuring the tip displacement has a noise level of ± 0.02 mm. For comparison purposes, a PI controller

$$K_1(s) = 3000\left(1 + \frac{1}{s}\right)$$

was also implemented together with a low-pass filter

$$F(s) = \frac{961}{s^2 + 62s + 961}$$

for the output measurement. Note that a PID controller was explored for IPMC actuators by Richardson *et al.* [30].

Fig. 13 shows the IPMC tracking performance under model-based H_∞ control and Fig. 14 shows the tracking performance under PI control. Simulation results under both PI control and H_∞ control are also shown in the figures. It can be seen that

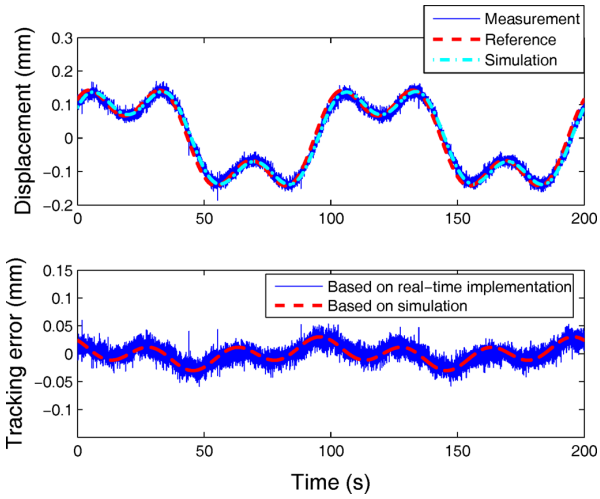

Fig. 14. Experimental and simulation results on tracking of IPMC actuator under PI control.

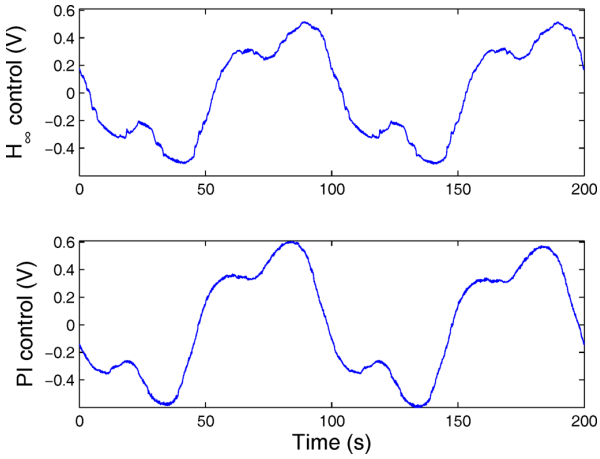

Fig. 15. Comparison of controller outputs under H_∞ control and PI control.

the tracking error under H_∞ control is almost at the level of sensing noise, while the error under PI control is about twice as large. The agreement between experimental and simulation results has further validated the reduced model. Fig. 15 compares the controller output under H_∞ control and PI control in the experiments, which shows that the H_∞ control requires lower control effort. Therefore, controller design based on the reduced model is effective.

VIII. Conclusion and Future Work

In this paper, a dynamic model for IPMC actuators was developed by solving the physics-governing PDE analytically in the Laplace domain. It is distinguished from existing modeling work of IPMC actuators in that it is amenable to model reduction and control design while capturing fundamental physics. The modeling work bridges the traditional gap between the physics-based perspective and the system-theoretic perspective on these novel but sophisticated materials. The model also incorporates the effect of surface electrode resistance in an integrative manner. The compact, explicit, transfer-function representation of the physics-based model can be reduced to low-order models for real-time feedback control purposes. A number of experimental results were presented to demonstrate the geometric scalability of the model. Due to the physical nature of the model, the agreement between model predictions and experimental results also provides insight into the underlying actuation mechanisms of IPMC materials. An H_∞ controller based on the reduced low-order model has been designed and implemented in real-time tracking experiments. Experimental results have proven that the proposed model is faithful and suitable for control design. Note that while this paper is focused on a particular class of smart materials, pursuing physics-based and control-oriented models could be a valuable approach to the design and control of a variety of materials and manufacturing systems [31].

Future work will be focused on two aspects. First, the proposed actuation model will be extended to incorporate material nonlinearities that become pronounced at large actuation levels. The nonlinearities include nonlinear elasticity, hysteresis [32], and the dependence of parameters (such as surface resistance) on the curvature output [24]. The actuation model in this paper was assumed to be a cascade of stress-generation module $H(s)$ and linear beam dynamics $G(s)$. However, the two-way coupling effects existing between the stress-generation module and the beam dynamics module, as indicated by the curvature-dependent electrical parameters, introduce challenging nonlinearities in modeling and control of IPMC materials that require further study. The second direction of future work is the application of the proposed modeling approach to control of micromanipulation [10] and biomimetic robots [9], [33]. There the model has to be extended to account for force interactions with external objects.

Appendix I
Derivation of Impedance Model (24)

From (21) and (22)

$$i_p(z,s) = \frac{\phi(h,z,s)}{h}\frac{sW\kappa_e\gamma(s)(s+K)}{(\gamma(s)s+K\tanh(\gamma(s)))} = \left(\frac{V(s)}{2} - \int_0^z \frac{r_1'}{W} i_s(\tau,s)\,d\tau - \frac{r_2'}{W} i_p(z,s)\right)\theta(s)$$

where the second equality is from (20) and (27). This results in

$$i_p(z,s) = \left(\frac{V(s)}{2} - \int_0^z \frac{r_1'}{W} i_s(\tau,s)\,d\tau\right)\frac{\theta(s)}{1+r_2\theta(s)}. \quad (46)$$

From (19) and (23), one obtains

$$i_k(z,s) = \frac{\phi(h,z,s) - \phi(-h,z,s) + 2i_p(z,s)r_2'/W}{R_p'/W} = \frac{2\phi(h,z,s) + 2i_p(z,s)r_2'/W}{R_p'/W} = \frac{2W}{R_p'}\left(\frac{V(s)}{2} - \int_0^z \frac{r_1'}{W} i_s(\tau,s)\,d\tau\right) \quad (47)$$

where the last equality is from (20).

Combining (18), (46), and (47), one gets

$$-\frac{\partial i_s(z,s)}{\partial z} = \frac{A(s)V(s)}{2} - B(s)\int_0^z i_s(\tau,s)\,d\tau \qquad (48)$$

where $A(s)$ and $B(s)$ are as defined in (25) and (26).

Equation (48) is an integrodifferential equation for i_s. To solve this equation, we introduce the unilateral Laplace transform for functions of the length coordinate z. The new Laplace variable will be denoted as p since s has already been used for the transform of time functions. For instance, the transform of $i_s(z,s)$ will be defined as

$$I_s(p,s) \triangleq \int_0^\infty i_s(z,s)e^{-pz}\,dz.$$

Now perform the Laplace transform with respect to the z variable on both sides of (48). Using properties of Laplace transforms, one gets

$$pI_s(p,s) - i_s(0,s) = -\frac{A(s)V(s)}{2}\frac{1}{p} + B(s)\frac{I_s(p,s)}{p}. \qquad (49)$$

Solving for $I_s(p,s)$, one obtains

$$I_s(p,s) = \frac{p}{p^2 - B(s)}i_s(0,s) - \frac{1}{p^2 - B(s)}\frac{A(s)V(s)}{2} \qquad (50)$$

which can be rewritten through partial fraction expansion as

$$I_s(p,s) = \frac{A(s)V(s)}{2}\left(\frac{q_1(s)}{p-\sqrt{B(s)}} + \frac{q_2(s)}{p+\sqrt{B(s)}}\right) + i_s(0,s)\left(\frac{0.5}{p-\sqrt{B(s)}} + \frac{0.5}{p+\sqrt{B(s)}}\right) \qquad (51)$$

with

$$q_1(s) = -\frac{1}{2\sqrt{B(s)}}, \qquad q_2(s) = \frac{1}{2\sqrt{B(s)}}.$$

The surface current $i_s(z,s)$ is then obtained from (51) using the inverse Laplace transform of $I_s(p,s)$

$$i_s(z,s) = i_s(0,s)\cosh\left(\sqrt{B(s)}z\right) - \frac{A(s)V(s)}{2\sqrt{B(s)}}\sinh\left(\sqrt{B(s)}z\right). \qquad (52)$$

Using the boundary condition $i_s(L,s) = 0$, one obtains

$$i_s(0,s) = \frac{V(s)A(s)\tanh\left(\sqrt{B(s)}L\right)}{2\sqrt{B(s)}}. \qquad (53)$$

REFERENCES

[1] M. Shahinpoor and K. Kim, "Ionic polymer–metal composites. Part I. Fundamentals," *Smart Mater. Struct.*, vol. 10, pp. 819–833, 2001.

[2] Y. Bar-Cohen, "Electric flex," *IEEE Spectr.*, vol. 41, no. 6, pp. 29–33, Jun. 2004.

[3] K. J. Kim and M. Shahinpoor, "Ionic polymer–metal composites. Part II. Manufaturing techniques," *Smart Mater. Struct.*, vol. 12, pp. 65–79, 2003.

[4] S. Tadokoro, S. Yamagami, and M. Ozawa, "Soft micromanipulation device with multiple degrees of freedom consisting of high polymer gel actuators," in *Proc. IEEE Int. Conf. Micro Electro Mech. Syst.*, 1999, pp. 37–42.

[5] S. Guo, T. Fukuda, and K. Asaka, "A new type of fish-like underwater microrobot," *IEEE/ASME Trans. Mechatron.*, vol. 8, no. 1, pp. 136–141, Mar. 2003.

[6] B. Kim, J. Ryu, Y. Jeong, Y. Tak, B. Kim, and J.-O. Park, "A ciliary based 8-legged walking micro robot using cast IPMC actuators," in *Proc. IEEE Int. Conf. Robots Autom.*, 2003, pp. 2940–2945.

[7] M. Shahinpoor and K. Kim, "Ionic polymer–metal composites. Part IV. Industrial and medical applications," *Smart Mater. Struct.*, vol. 14, pp. 197–214, 2005.

[8] M. Yamakita, N. Kamamichi, T. Kozuki, K. Asaka, and Z. Luo, "Control of biped walking robot with IPMC linear actuator," in *Proc. IEEE/ASME Int. Conf. Adv. Intell. Mechatron.*, Monterey, CA, 2005, pp. 48–53.

[9] X. Tan, D. Kim, N. Usher, D. Laboy, J Jackson, A Kapetanovic, J. Rapai, B. Sabadus, and X. Zhou, "An autonomous robotic fish for mobile sensing," in *Proc. IEEE/RSJ Int. Conf. Intell. Robots Syst.*, Beijing, China, 2006, pp. 5424–5429.

[10] Z. Chen, Y. Shen, N. Xi, and X. Tan, "Integrated sensing for ionic polymer–metal composite actuators using PVDF thin films," *Smart Mater. Struct.*, vol. 16, pp. S262–S271, 2007.

[11] J. W. L. Zhou, H.-Y. Chan, T. K. H. To, K. W. C. Lai, and W. J. Li, "Polymer MEMS actuators for underwater micromanipulation," *IEEE/ASME Trans. Mechatron.*, vol. 9, no. 2, pp. 334–342, Jun. 2004.

[12] R. Kanno, A. Kurata, S. Tadokoro, T. Takamori, and K. Oguro, "Characteristics and modeling of ICPF actuator," in *Proc. Japan-USA Symp. Flexible Autom.*, 1994, pp. 219–225.

[13] N. D. Bhat, "Modeling and precision control of ionic polymer metal composite" M.S. thesis, Texas A&M University, Arlington, 2003.

[14] R. Kanno, S. Tadokoro, T. Takamori, and M. Hattori, "Linear approximate dynamic model of IPMC (ionic conducting polymer gel film) actuator," in *Proc. IEEE Int. Conf. Robot. Autom.*, Minneapolis, MN, 1996, pp. 219–225.

[15] K. M. Newbury and D. J. Leo, "Linear electromechanical model for ionic polymer transducers. Part I. Model development," *J. Intell. Mater. Syst. Struct.*, vol. 14, pp. 333–342, 2003.

[16] C. Bonomo, L. Fortuna, P. Giannone, S. Graziani, and S. Strazzeri, "A nonlinear model for ionic polymer metal composites as actuators," *Smart Mater. Struct.*, vol. 16, pp. 1–12, 2007.

[17] P. G. de Gennes, K. Okumura, M. Shahinpoor, and K. Kim, "Mechanoelectric effects in ionic gels," *Europhys. Lett.*, vol. 50, no. 4, pp. 513–518, 2000.

[18] S. Nemat-Nasser and J. Li, "Electromechanical response of ionic polymer–metal composites," *J. Appl. Phys.*, vol. 87, no. 7, pp. 3321–3331, 2000.

[19] S. Tadokoro, S. Yamagami, T. Takamori, and K. Oguro, "Modeling of Nafion–Pt composite actuators (ICPF) by ionic motion," in *Proc. SPIE*, 2000, pp. 3987-1–3987-15.

[20] K. M. Farinholt, "Modeling and characterization of ionic polymer transducers for sensing and actuation," Ph.D. dissertation, Virginia Polytechnic Inst. State Univ., Blacksburg, 2005.

[21] P. J. Costa Branco and J. A. Dente, "Derivation of a continuum model and its electric equivalent-circuit representation for ionic polymer–metal composite (IPMC) electromechanics," *Smart Mater. Struct.*, vol. 15, pp. 378–392, 2006.

[22] Y. W. Yang and L. Zhang, "Modeling of dynamic behaviors of ionic polymer–metal composites," presented at the World Forum Smart Mater. Smart Struct. Technol., Chongqing and Nanjing, China, 2007.

[23] M. Shahinpoor and K. J. Kim, "The effect of surface-electrode resistance on the performance of ionic polymer–metal composite (IPMC) artificial muscles," *Smart Mater. Struct.*, vol. 9, pp. 543–551, 2000.

[24] A. Punning, M. Kruusmaa, and A. Aabloo, "Surface resistance experiments with IPMC sensors and actuators," *Sens. Actuators A*, vol. 136, pp. 656–664, 2007.

[25] S. Nemat-Nasser, "Micromechanics of actuation of ionic polymer–metal composites," *J. Appl. Phys.*, vol. 92, no. 5, pp. 2899–2915, 2002.

[26] J. M. Gere and S. Timoshenko, *Mechanics of Materials*. 4th ed. Boston, MA: PWS-Kent, 1997.

[27] E. Voltera and E. C. Zachmanoglou, *Dynamics of Vibrations*. Indianapolis, IN: Charles E. Merrill Books, 1965.

[28] G. A. Baker and P. Graves-Morris, *Padé Approximants*. New York: Cambridge Univ. Press, 1996.

[29] K. Zhou, *Essentials of Robust Control*. Upper Saddle River, NJ: Prentice-Hall, 1998.

[30] R. C. Richardson, M. C. Levesley, M. D. Brown, J. A. Hawkes, K. Watterson, and P. G. Walker, "Control of ionic polymer metal composites," *IEEE/ASME Trans. Mechatron.*, vol. 8, no. 2, pp. 245–253, Jun. 2003.

[31] K.-M. Lee, Z. Wei, and Z. Zhou, "Modeling by numerical reduction of modes for multivariable control of an optical-fiber draw process," *IEEE Trans. Autom. Sci. Eng.*, vol. 3, no. 1, pp. 119–130, Jan. 2006.
[32] Z. Chen, X. Tan, and M. Shahinpoor, "Quasi-static positioning of ionic polymer–metal composite (IPMC) actuators," in *Proc. IEEE/ASME Int. Conf. Adv. Intell. Mechatron.*, Monterey, CA, 2005, pp. 60–65.
[33] E. Mbemmo, Z. Chen, S. Shatara, and X. Tan, "Odeling of biomimetic robotic fish propelled by an ionic polymer–metal composite actuator," in *Proc. 2008 IEEE Int. Conf. Robot. Autom.*, Pasadena, CA, pp. 689–694.

Zheng Chen (S'05) received the B.S. degree in electrical engineering and the M.S. degree in control science and engineering from Zhejiang University, Hangzhou, China, in 1999 and 2002, respectively. He is currently working toward the Ph.D. degree in electrical and computer engineering at Michigan State University (MSU), East Lansing.

His current research interests include modeling and control of electrical-active polymers (EAPs), EAP-based smart microsystems, control of dynamical systems with hysteresis, and neural networks.

Mr. Chen was the recipient of a Summer Dissertation Fellowship from MSU Graduate School in 2005, and an Honorable Mention for the Fitch Beach Outstanding Graduate Research Award from MSU College of Engineering in 2008.

Xiaobo Tan (S'97–M'02) received the Bachelor's and Master's degrees in automatic control from Tsinghua University, Beijing, China, in 1995 and 1998, respectively, and the Ph.D. degree in electrical and computer engineering from the University of Maryland, College Park, in 2002.

From September 2002 to July 2004, he was a Research Associate at the Institute for Systems Research (ISR), University of Maryland. He is currently an Assistant Professor in the Department of Electrical and Computer Engineering, Michigan State University, East Lansing. His current research interests include electroactive polymer sensors and actuators modeling and control of smart materials, biomimetic robotics, bio/micromanipulation, and collaborative control of unmanned vehicles.

Dr. Tan was a recipient of the National Science Foundation CAREER Award in 2006.